AXUV synthetic diagnostic for ASDEX Upgrade and its application for SPI simulations

F. Lengyel[1,2], W. Tang[3], M. Hölzl[3,4], M. Bernert[3], M. Tomeš[5], P. Halldestam[3], P. Heinrich[3], G. Papp[3], S. Jachmich[6], U. Sheikh[7], M. Dibon[5], P. de Marné[3], J. Hobirk[3], T. Eberl[3], G. I. Pokol[1,2], the ASDEX Upgrade Team[a] and the EUROfusion Tokamak Exploitation Team[b]

[1] HUN-REN Centre for Energy Research, Institute for Atomic Energy Research, Budapest, Hungary
[2] Department of Nuclear Techniques, Budapest University of Technology and Economics, Budapest, Hungary
[3] Max Planck Institute for Plasma Physics, Garching, Germany
[4] Department of Physics and Astronomy, Chalmers University of Technology, Göteborg, SE-41296, Sweden
[5] Institute of Plasma Physics, Czech Academy of Sciences, Prague, Czech Republic
[6] ITER Organization, Saint Paul Lez Durance, France
[7] Swiss Plasma Center, EPFL, Lausanne, Switzerland
[a] See the author list of T. Pütterich et al. 2026 Nucl. Fusion 66 116002
[b] See the author list of N. Vianello et al. 2026 Nucl. Fusion 66 116010

1. Motivation

AXUV diodes detect electromagnetic radiation across a wide spectral range, from the visible to the soft X-ray, at a time resolution (~μs) higher than that of foil bolometers (~ms) [1]. This makes them well suited to measuring fast phenomena such as shattered pellet injection (SPI), where the spatial localisation and the radiated power of the emission carry information about the deposition of the pellet material. The use of AXUV diodes for quantitative radiation measurements is, however, limited by a non-uniform spectral responsivity that degrades during plasma operation, as VUV photons damage the entrance window of the diodes [2]. The nominal and the measured (after a campaign) degraded spectral responsivities are shown in Figure 1. During the 2022 AUG SPI campaign, more than half of the launched pellets contained neon, which radiates throughout the sensitive spectral range of the diodes. Even if the diodes were calibrated to standard plasma experiments, the dominant neon line spectrum invalidates the calibration and makes the absolute power determination susceptible to systematic error. A further challenge is that, in a neon-doped shattered-pellet induced disruption, the emitted spectrum changes substantially as the plasma cools, so the effective response of a diode (the responsivity weighted by the incident spectrum) is expected to change throughout the discharge in the range of ~0.1 – 0.26 AW^{-1} [3].

This paper highlights the main results of a recent study [3] on a three-dimensional synthetic AXUV diagnostic developed to support radiation feature comparison: to connect higher-fidelity plasma simulations with the measured signals and thereby to help validate the simulations and the physical models used within. We summarise the implementation, verification, and a first application to a JOREK SPI simulation.

2. The 3D synthetic diagnostic

The diagnostic is built on Cherab [4,5], an open-source library for spectroscopic diagnostic modelling, and the underlying Raysect ray-tracing framework [6]. The AUG AXUV diodes are represented as detectors placed inside camera boxes with rectangular slits, with positions and orientations taken from the AUG shotfiles. Four cameras are modelled at two toroidal sectors: the vertical cameras D16 (sector 16) and DVC (sector 5), and the horizontal cameras DHT (sector 16) and DHC (sector 5). Each camera consists of three arrays of sixteen 2 mm × 5 mm diodes, for a total of 192 lines of sight; all four view the full poloidal cross-section, with the longer diode side aligned toroidally. The lines of sight of the two sector 16 camreas are shown in the poloidal cross-section of AUG in Figure 2. Sector 16 hosts the SPI, while sector 5 is located ~110° away toroidally, which allows the radiation to be compared at two toroidal locations. The vessel wall surrounding the diodes is represented either by a simple toroidal absorbing surface or, for the reflection calculations, by the full CAD geometry of the AUG plasma-facing components, treated as rough tungsten (a material type defined in Cherab).

The spatial sensitivity of each detector channel is computed using the ray transfer method [7]: the plasma volume is described by an axisymmetric toroidal voxel grid, and 10^6 rays are traced from each diode, through the camera slit and the voxels, to the surrounding surfaces (and further,

across several passes, if those surfaces reflect). This gives, for each line of sight, a sensitivity matrix giving the contribution of each voxel to that channel, which is later multiplied by the per-voxel emission of the plasma in Cherab to obtain the power on the diode. This is useful if the geometry is static and the emission has time evolution. A 2 cm × 2 cm voxel resolution was used in the radial and vertical dimensions. A 1 cm × 1 cm test gave differences below 5% on average, which is small compared to the four orders of magnitude spanned by the experimental signals during Ne-doped SPI disruptions.

The spectral simulation was performed on the energy range 1 eV – 1.24 keV. Since Raysect, the raytracing framework Cherab is built on, uses Spectrum objects with linear binning in wavelength, the examined spectral range was divided into three regions: 1 – 10 eV, 10 – 100 eV, and 100 – 1240 eV. Three independent, 100-bin Spectrum objects were set up on the three regions, yielding 300 total spectral bins. When using the reflecting tungsten wall, the aforementioned sensitivity matrix calculation is performed 300 times to account for spectrally dependent reflections. The plasma emission is computed with Cherab from post-processed JOREK output; the simulations used here did not include neutral deuterium, so only Bremsstrahlung and neon line radiation (from OPEN-ADAS) were modelled. For the reflection calculations, the wavelength-dependent refractive index and extinction coefficient of the tungsten components are taken from the Cherab defaults across the visible range and extrapolated into the soft X-ray range based on [7,8]. The reflected contribution is most apparent in the edge channels but provides a general background for all diodes.

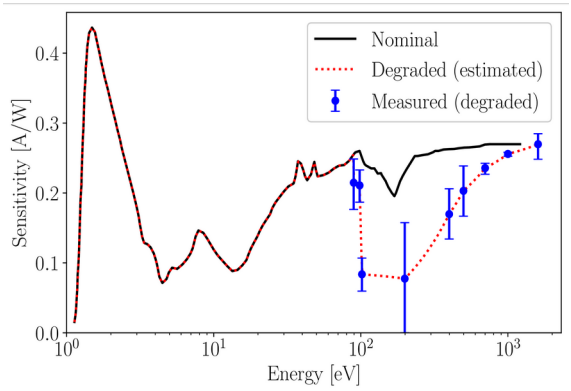

Figure 1 — AXUV spectral responsivity: the manufacturer-specified nominal curve and the post-campaign degraded curve used here [1].

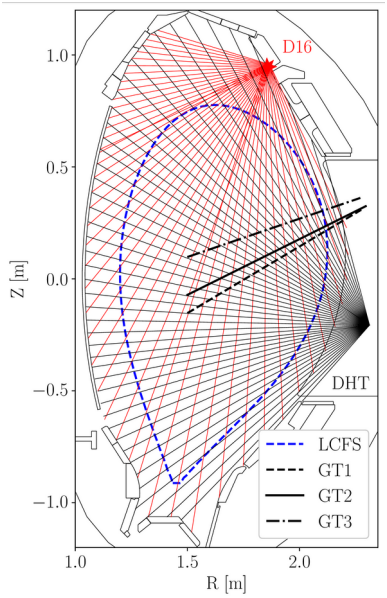

Figure 2 — AUG poloidal cross-section with the sector-16 vertical (D16) and horizontal (DHT) lines of sight, a typical H-mode LCFS, and the SPI guide-tube vectors.

3. Verification

The line-of-sight geometry was verified against the AUG data: the modelled lines of sight overlap those exported from the shotfiles. The diode etendues were compared with the analytic values calculated at AUG and a good match was found, with a mean relative difference of 2.3% (maximum 7.09%). The differences in the etendues likely stem from the ray-tracing accounting for half-shadows, which the analytic formula does not. The ray transfer method was further cross-checked against another approach available in Cherab, in which the power reaching each diode is obtained by sampling the plasma emission along rays traced from the diode (PowerPipeline). For homogeneous emission on the same voxel geometry, the mean relative error in the observed channel power was 0.017% (maximum 2.44%).

Validation against standard plasma discharges is, by contrast, more difficult, mainly because of tungsten: its concentration is hard to measure accurately, its atomic data are incomplete, and it radiates strongly in the VUV–SXR range, where the diode sensitivity degrades the most during

operation [1]. We therefore use neon-deuterium mixed SPI as the test case, since the radiation from the injected impurity is much stronger than the intrinsic radiation, so that order-unity uncertainties in the relative effective sensitivity between channels do not invalidate a comparison of radiation features. Additionally, 3D modeling is motivated to be able to disentangle the effects of the toroidally symmetric background impurity radiation and the toroidally asymmetric radiation and the reflections of that radiation from the neon in the pellet cloud.

4. Application to a JOREK SPI simulation

Non-linear three-dimensional JOREK SPI simulations were performed for two AUG discharges, as presented in [10], that reproduce several global plasma parameters and their time evolution with good quantitative agreement. Three comparisons were performed using the synthetic diagnostic on the simulation output (sectors 16 and 5 for discharge #40673, and sector 16 for the trace-neon discharge #41007). The sector-16 comparison for #40673 is shown here; the others are reported in [3]. In discharge #40673, the pellet contained 10 mol% Ne and 90 mol% D_2. The degraded responsivity was used for the synthetic diagnostic and reflections switched on. At this neon content, both the plasmoid drift [11] and the rocket effect [11,12] acting on the shards are expected to be relatively weak, so the trajectory of the radiating cloud should approximately match the shard trajectories.

Figure 3 compares the synthetic (top) and experimental (bottom) line-integrated brightness for every channel of the sector-16 vertical and horizontal cameras. The time axes are aligned to the arrival of the first pellet shards, and the times $t_{0.8W}$ and $t_{0.2W}$ are marked, at which the thermal energy reaches 80% and 20% of its initial value. These are useful physics-based reference points for the thermal quench [14], the duration of which is largely determined by the radiative losses observed by the AXUV diagnostic. The initial inward penetration of the radiation cloud shows a good match in both velocity and amplitude until about t = 2.3285 s, consistent with the expected trajectory matching at higher neon content. Fine radiation structures shooting off of the main cloud towards the high-field side appear in both datasets, and together with the horizontal-camera signals they suggest that the radiation spreads along the outer flux surfaces, vertically downward and towards the high-field side.

After t = 2.3285 s, the synthetic vertical signal shows a single abrupt radial spreading of the cloud, whereas in the experiment several smaller events are seen; the evolution of the spatial extent of the cloud nonetheless appears qualitatively consistent between the two. Some of the difference is expected: pellet shattering is an inherently stochastic process, the fragment number and velocity distributions are not known precisely, and the JOREK run did not include intrinsic impurities, so the background in the synthetic data is due to reflections alone, whereas the experiment also contains intrinsic impurities such as tungsten. Since the pellet carries a relatively large amount of neon, its radiation dominates, and the intrinsic impurity radiation remains less significant for this discharge. After the thermal energy drops below 20% of its initial value, the fine structures are quickly smoothed out in both datasets, which may indicate significant mixing. Overall, the synthetic data reproduce the experimental features qualitatively, and some features quantitatively, confirming that the diagnostic is a suitable tool for this kind of comparison.

5. Summary

A three-dimensional synthetic AXUV diagnostic has been developed for ASDEX Upgrade in the Cherab/Raysect framework, covering 192 lines of sight in four cameras across two toroidal sectors, with the full CAD geometry of the tungsten plasma-facing components used to compute wavelength-dependent reflections. The diagnostic has been verified against the AUG line-of-sight geometry, the analytically calculated etendue values, and an independent power-sampling method in Cherab. Its first application, to a JOREK SPI simulation of AUG discharge #40673 (10 mol% Ne), gives qualitatively and in some cases even quantitatively good agreement between the synthetic and experimental AXUV signals in the SPI sector. This suggests that the synthetic diagnostic can be used to connect high-fidelity plasma simulations with AXUV measurements and

to help validate both the simulations and their physics inputs. The synthetic diagnostic can also be adapted to other devices with similar diagnostic systems. A more detailed comparison, including the second toroidal sector and a trace-neon discharge in which the plasmoid drift and the rocket effect become more important, is presented in the companion paper [3].

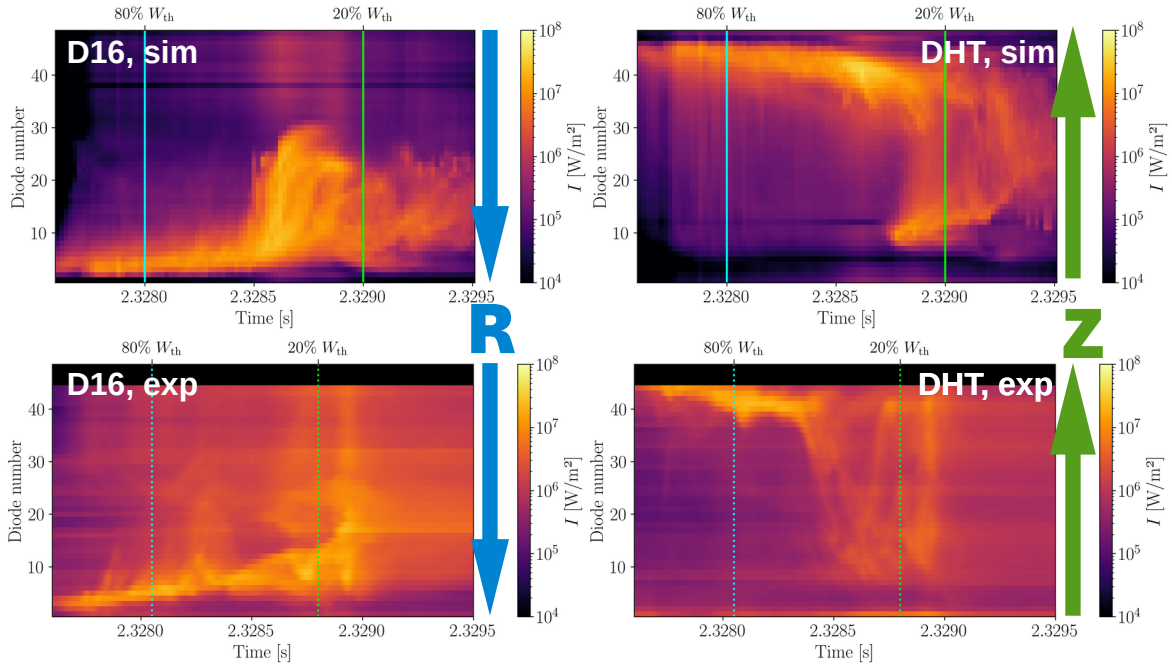

[Figure 3 — Synthetic (top) and experimental (bottom) AXUV line-integrated brightness for the sector-16 vertical (D16) and horizontal (DHT) cameras of AUG discharge #40673 (10 mol% Ne). The same logarithmic colour scale is used for all panels; $t_{0.8W}$ and $t_{0.2W}$ are marked (solid for the simulation, dotted for the experiment).]

Acknowledgements

This work has been carried out within the framework of the EUROfusion Consortium, funded by the European Union via the Euratom Research and Training Programme (Grant Agreement No 101052200 — EUROfusion). Views and opinions expressed are however those of the author(s) only and do not necessarily reflect those of the European Union or the European Commission. Neither the European Union nor the European Commission can be held responsible for them. F. Lengyel acknowledges the support of the JNEA Foundation.

References

[1] Bernert, M. *et al. Rev. Sci. Instrum.* **85**, 033503 (2014).
[2] Tál, B. PhD thesis, Budapest University of Technology and Economics, Budapest, Hungary (2015).
[3] Lengyel, F. *et al.* AXUV synthetic diagnostic for ASDEX Upgrade and its application for SPI simulations. To be submitted to *J. Plasma Phys.* (2026).
[4] Carr, M. *et al.* In proceedings of 44th EPS Conference on Plasma Physics vol. 41F, Belfast, Northern Ireland (UK), (2017).
[5] Carr, M. *et al.* cherab/core v1.4.0 Release https://doi.org/10.5281/zenodo.7603688 (2023).
[6] Meakins, D. A. *et al.* raysect/source v0.8.0 Release https://doi.org/10.5281/zenodo.7633656 (2023).
[7] Kajita, S., Veshchev, E., Barnsley, R. & Walsh, M. *Contrib. Plasma Phys.* **56**, 837–845 (2016).
[8] Windt, D. L. *et al. Appl. Opt.* **27**, 246–278 (1988).
[9] Polyanskiy, M. N. *Sci. Data* **11**, 94 (2024).
[10] Tang, W. *et al.* Submitted to *Nucl. Fusion* Preprint at https://doi.org/10.48550/arXiv.2602.12813 (2026).
[11] Kong, M. *et al. Plasma Phys. Control. Fusion* **68**, 065016 https://doi.org/10.1088/1361-6587/ae72c7 (2026).
[12] Corbett, J. *et al.* Submitted to *Plasma Phys. Control. Fusion* Preprint at https://doi.org/10.48550/arXiv.2512.04484 (2026).
[13] Vallhagen, O., Pusztai, I., Helander, P., Newton, S. L. & Fülöp, T. *J. Plasma Phys.* **89**, 905890306 (2023).
[14] Artola, F. J. *et al. arXiv.org* https://arxiv.org/abs/2604.22516v1 (2026).